The Influence of Catalyst Chemical State and Morphology on Carbon Nanotube Growth

Teresa de los Arcos,*,† Michael Gunnar Garnier,†,‡ Jin Won Seo,§ Peter Oelhafen,† Verena Thommen,† and Daniel Mathys‖

*Institute of Physics, University of Basel, Klingelbergstrasse 82, CH-4056 Basel, Switzerland,
Institute of Physics of Complex Matter, EPFL, Ecublens, CH-1015 Lausanne, Switzerland, and
Zentrum für Mikroskopie, University of Basel, Klingelbergstrasse 50/70, CH-4056 Basel, Switzerland*

Carbon nanotubes grown by chemical vapor deposition have revealed differences in growth rate and characteristics depending on the underlying buffer layer. As determined by in situ photoelectron spectroscopy, iron catalyst deposited onto Si substrates covered with Al_2O_3, TiN, or TiO_2 underwent different chemical changes during annealing and exposure to C_2H_2 as function of buffer layer. Formation of thin tubes (2–4 walls) and fast growth rate were associated with conversion of Fe onto FeO particles on Al_2O_3 layers. On the other hand, thick multiwalled tubes (more than 20 walls) grew from pure Fe particles formed onto TiN and TiO_2 layers. The influence of different buffer layers is attributed to a combination of chemical and morphological changes induced in the catalyst due to catalyst-substrate interaction.

1. Introduction

In the production of carbon nanotubes (CNTs) by chemical vapor deposition (CVD), control over CNT structure and growth is achieved through a plethora of experimental parameters such as process temperature, gas mixtures, pressure, flow rates, etc. One of the most important parameters however, is the catalyst employed, and the nature of the catalyst−substrate interaction. Although there is a consensus as to the importance of selecting the appropriate catalyst−substrate combination, there is still a degree of confusion as to the exact role played by the chemical composition and structure of the catalytic particles, since the precise CNT growth mechanism is still unknown. A generally accepted view is that growth of nanotubes from carbon containing gases is based on diffusion models in which, roughly, gas molecules decompose on the surface of metallic particles, C diffuses inside, and, when the catalyst particle saturates, C solute precipitates on the particle surface as crystalline graphite. In such cases, diffusion of carbon through the metallic particle is considered to be the rate-determining step.[1–3] However, these models fail to explain all accumulated experimental evidence in CNT production, particularly because the catalyst is assumed to be in metallic form, while in the vast amount of literature concerning CVD growth of CNTs, catalysts in different chemical states seem to be involved. The possibility of carbides participating in the growth has been reported,[4,5] as has that for oxides. Despite their absence in proposed growth models, oxides have been repeatedly reported to be effective for the formation of nanofibers. Baker et al., for example, compare the efficiency of bulk Fe, FeO, and Fe_2O_3 for growth of carbon filaments and found that FeO was the most active catalyst, while Fe and Fe_2O_3 had similar performances.[6] There are reports of cases where the original metallic catalyst oxidizes,[7] while in other cases, the

Fe_2O_3 clusters are directly employed as starting point.[8–11] One common view is that the oxidized particles are reduced during CVD, so that independently of the initial oxidation state, metal particles are the active catalyst form.[11] Following this interpretation, in some cases extra care is taken to ensure the reduction of the catalyst before CVD by exposure of the samples to reducing atmospheres, like for example hydrogen or ammonia plasmas. However, the actual composition of the catalyst involved in the growth is generally unknown.

The deposition of a thin buffer layer under the catalyst is a common practice in CVD growth of CNTs onto Si substrates, to avoid metal silicide formation at the high temperatures involved in the process.[12,13] However, the role of these intermediate layers is not merely passive, since it has been established that they can influence the growth and characteristics of the tubes.[14–17] We attribute the influence of different buffer layers to a combination of chemical and morphological changes induced in the catalyst due to catalyst−substrate interaction. In this work, we have undertaken a detailed in situ photoelectron spectroscopy (PES) study of the changes in chemical composition of an iron catalyst during the different stages of a typical CVD growth procedure, and the influence of the final catalyst chemical state on CNT structure and growth. We will show how, although the initial chemical state was always metallic, Fe underwent different chemical changes depending on the underlying buffer layers employed.

2. Experimental Setup

2.1. Setup I, for Chemical Analysis and CNT Growth. Two different experimental setups were used. The first one consists of a high vacuum chamber (background pressure $1 \cdot 10^{-6}$ mbar) adapted for carbon nanotube growth, attached to an ultrahigh vacuum (UHV) chamber housing a photoelectron spectrometer (Leybold EA10N). The Si (100) wafers used as substrates were rinsed in ultrasonic baths of acetone and ethanol for several minutes before introduction into the growth chamber, where they were mounted on a Mo sample holder that can be rotated to different positions. This allowed consecutive deposition of

* Corresponding author. E-mail: t.arcos@unibas.ch.
† Institute of Physics, University of Basel.
‡ Present address: Institute of Physics, University of Neuchâtel, rue Breguet 1, CH-2000 Neuchâtel, Switzerland.
§ Institute Physics of Complex Matter.
‖ Zentrum für Mikroskopie, University of Basel.

Influence of Catalyst Chemical State and Morphology

J. Phys. Chem. B, Vol. 108, No. 23, 2004 **7729**

different compounds onto the same sample without breaking the vacuum. Before the deposition of Fe catalyst, a buffer layer of Al_2O_3, TiN, or TiO_2 was deposited onto the Si substrate (covered with 2 nm thick native oxide layer) by magnetron sputtering. The thickness of the buffer layers was in all cases 20 nm, except for the TiN layers, where the thickness varied between 40 and 80 nm. In this case, the substrate had to be biased to a negative potential of −200 V in order to obtain a structure dense enough to act as a diffusion barrier for Fe.[12] Fe was deposited by ion beam sputtering of an Fe target with a Kaufman ion source. Except for TiN, the deposition rate was determined by a quartz crystal monitor. Once the catalyst had been deposited, the samples were heated in a vacuum (pressure during the annealing rises to $1-2 \cdot 10^{-5}$ mbar), reaching a final temperature of 840 °C in 8 min. The temperature was measured by means of a thermo element placed directly under the Si substrate. When the final temperature had been reached, acetylene gas (C_2H_2) was introduced into the chamber at controlled flow and pressure (35 sccm and 0.1 mbar), to start the CVD growth of CNTs. After each of the experimental steps described (deposition of buffer layer, catalyst, annealing, and CVD), the samples were allowed to cool to room temperature and transferred to the UHV chamber for X-ray photoelectron spectroscopy (XPS) analysis without breaking the vacuum. For XPS, Mg Kα excitation was employed, with a spectral resolution of 0.9 eV. The energy position of each spectrum was calibrated with reference to the $4f_{7/2}$ level of a clean gold sample, at 84.0 eV binding energy.

2.2. Setup II, for Chemical Analysis at High Temperature. This second experimental setup consists of an UHV chamber attached to a second UHV system with a photoelectron spectrometer. The spectrometer is a VG ESCALAB 210 equipped with a monochromatic Al Kα X-ray source giving an experimental resolution of 0.5 eV. The particularities of this setup are that the samples can be annealed in UHV conditions (pressure during annealing rises to $1 \cdot 10^{-8}$ mbar), and that XPS measurements of hot samples can be performed. This setup was not conditioned for CNT growth and was solely used to study the chemical changes underwent by the catalyst during annealing in an UHV environment.

2.3. Ex Situ Characterization Methods. The structure of buffer layers with and without Fe was investigated before and after the annealing step by atomic force microscopy (AFM, Digital Instruments, Dimension 3100, in tapping mode) and scanning electron microscopy (SEM, JEOL JSM 6300F, at 15 kV) in the secondary and backscattered modes. Analysis of CNTs was done with SEM and transmission electron microscopy (TEM, Philips CM20 and CM300).

3. Experimental Results

3.1. In Situ XPS Analysis of Catalyst Chemical Composition. *3.1.1. Catalyst Composition during and after Annealing in UHV (10^{-8} mbar).* Si wafers already covered with Al_2O_3, TiN and TiO_2 layers in setup I were transferred into setup II, where the catalyst (1 nm of clean Fe) was deposited onto the samples by means of a pulsed arc deposition source in a vacuum environment of $10^{-8}-10^{-7}$ mbar. After Fe deposition, the samples were transferred to the UHV measurement chamber without breaking the vacuum. They were then annealed to 840 °C and analyzed by XPS at this temperature. During annealing and measurement the background pressure rose to $1 \cdot 10^{-8}$ mbar in the UHV system.

In Figure 1 we can follow the chemical changes experienced by Fe from the behavior of the Fe 2p doublet as measured by
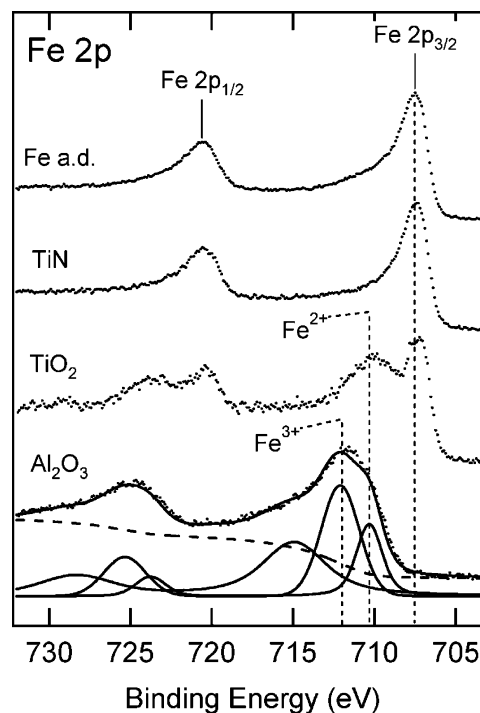

Figure 1. XPS (Al Kα) spectra of the Fe 2p core line of Fe as deposited by pulsed arc and measured at room temperature (upper trace) and during annealing to 840 °C under UHV conditions ($10^{-9}-10^{-8}$ mbar) onto buffer layers of TiN, TiO_2, and Al_2O_3. Spectra have been normalized to the same maximum intensity in order to facilitate comparison.

XPS. The upper trace shows a typical spectrum of Fe before annealing. The Fe deposited was in all cases chemically pure (Fe $2p_{3/2}$ line at 706.8 eV binding energy). However, during heating the chemical state of Fe changed in different ways as function of the underlying buffer layer. In the case of the TiN layer, no change in the Fe chemical state was observed and it remained as pure Fe. Furthermore, experiments realized with previously oxidized Fe (not presented here) showed how iron oxide was always reduced to pure iron during the annealing on TiN layers under UHV conditions. In contrast, Fe annealed onto TiO_2 layers underwent a partial oxidation, as can be seen in the spectrum by the appearance of a contribution corresponding to an Fe^{2+} oxidation state (FeO), at 709.7 eV binding energy (BE). During annealing of Fe onto Al_2O_3 layers, Fe was completely oxidized, showing a mixture of Fe^{2+} (709.7 eV) and Fe^{3+} (711.9 eV) oxidation states. In this latter case, a fit was performed assuming a convolution of Gaussian and Lorentzian line shapes and a Shirley background. Next to the two oxide components, it was necessary to consider a third peak in order to take into account the shake-up satellites associated to Fe^{2+} and Fe^{3+} oxidation states,[18,19] which are not resolved in this spectrum. After measurement, the samples were allowed to cool to room temperature and measured again (not shown), but the chemical changes were irreversible, and no change in Fe composition was observed with respect to the high-temperature case. This is of relevance, since all XPS measurements described in the next section were done after cooling the samples to room temperature.

3.1.2. Catalyst Composition after Annealing in HV (10^{-5} mbar) and after CVD. In the experiments described in this section, deposition of buffer layer, deposition of catalyst, annealing, and exposure to C_2H_2 are performed sequentially in setup I, without breaking the vacuum. In the XPS spectra shown in Figure 2 we can follow the evolution of the chemical state
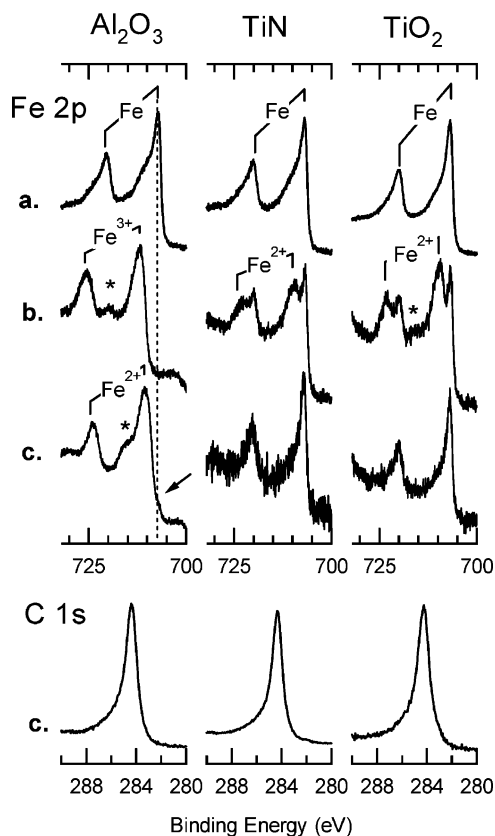
Figure 2. Evolution of the XPS (Mg Kα) spectra of the Fe 2p line for different stages of the growth procedure, onto Si wafers covered with buffer layers of Al_2O_3, TiN and TiO_2. (a) 1 nm Fe measured before annealing (as-deposited). (b) After annealing in a vacuum (10^{-5} mbar) up to 840 °C during 8 min. (c) After annealing the samples during 8 min and then exposing them to C_2H_2 for 5 s in order to initiate CNT growth. All spectra have been normalized to the maximum intensity in order to facilitate comparison. The lower row shows the C 1s core level line of the samples after the 5 s exposure to C_2H_2.

of Fe deposited onto the different buffer layers at different stages of the CNT growth process.

Fe as Deposited: The first row of spectra (a) in Figure 2 corresponds to Fe as deposited onto the three different buffer layers by ion beam sputtering. In all cases, the position of the Fe $2p_{3/2}$ line corresponds to pure Fe (706.8 eV), with a shoulder at approximately 710 eV indicative of a small amount of oxidized Fe.

Fe after Annealing: The second row of spectra (b) shows the chemical state of Fe after annealing the samples in a vacuum (background pressure during annealing $1-2 \cdot 10^{-5}$ mbar) up to the process temperature during a time of 8 min, equivalent to the preheating time in the CVD process. Heating was stopped at the moment when C_2H_2 would have been introduced into the chamber to initiate CNT growth, and samples cooled in a vacuum to room temperature before XPS measurement. As discussed in the previous section, significant differences in chemical state can be seen as a function of the buffer layer. However, due to the higher background pressure in setup I, oxidation of Fe is in general more pronounced than for the UHV annealing in setup II. Therefore, even Fe annealed onto TiN layers underwent a partial oxidation. The component at 709.7 eV BE, which corresponds to FeO is clearly present for TiN and TiO_2 together with its corresponding shake-up satellite (marked with an asterisk *) at approximately 715 eV.[19] Fe annealed onto Al_2O_3 buffer layers underwent again a complete oxidation, but in this case to the higher oxidation state Fe^{3+}

(with Fe $2p_{3/2}$ position at 711.9 eV and shake up satellite at 720 eV) with no apparent contribution from Fe^{2+}. Additionally, there is in all cases a certain loss of Fe 2p peak intensity that can be attributed to several factors, like Fe reorganizing on the surface or Fe diffusing inside the substrate. However, the spectra have been normalized in order to facilitate comparison.

Fe after CVD: In the third row of spectra (c) of Figure 2 we can see the chemical state of Fe after annealing during 8 min followed by exposure to C_2H_2 for approximately 5 s. Longer exposures lead to the total coverage of the surface by CNTs, so that the only signal detected with XPS was that of carbon. Spectra shown here were normalized for comparison to compensate the intensity loss due to carbon coverage. Due probably to the presence of hydrogen species liberated during the catalytic decomposition of C_2H_2, a reduction of Fe is observed with respect to the chemical state seen after the annealing step. In the case of TiN and TiO_2 buffer layers, this reduction means a complete reversion to pure Fe, while in the case of the Al_2O_3 layer only a partial reversion occurs, with a transformation from Fe^{3+} to Fe^{2+}. Although iron carbide formation has been reported in other works,[4,5] we found no evidence of carbide formation in the XPS analysis of our cooled samples, either in the Fe 2p or in the C 1s lines, which can be seen at the bottom row of the spectra in Figure 2. The position of the C 1s lines (at 284.3 eV BE) corresponded to CNTs.

3.2. Ex Situ Analysis of Substrates and Nanotubes. *3.2.1. Catalyst Redistribution after Annealing.* After determination of the chemical composition of Fe, the surface morphology of annealed and not annealed samples was investigated with AFM and SEM. AFM measurements presented in Figure 3 show changes in the surface morphology of the different buffer layers covered with 1 nm Fe before (a) and after annealing (b). Case c corresponds to buffer layers annealed without Fe in order to distinguish changes due to Fe reorganization from possible changes occurring in the layers themselves.

The surface of the Fe-covered samples (case b) shows in all cases a rougher appearance after annealing. Since Al_2O_3 and TiO_2 layers possess a smooth surface after annealing (case c.), it is reasonable to assume that the surface structure of the samples in these two cases is due to the formation of iron and/ or iron oxide clusters. However, in the case of TiN layers it is difficult to disentangle information concerning Fe particle formation due to the inherent rough surface of the films.[20] Therefore, secondary and backscattered SEM images of the Fe-containing annealed TiN sample were performed, as can be seen in Figure 4. The secondary image (left) provides topography information, like in the case of AFM measurements. The backscattered image (right) provides element contrast information. When measuring in the backscattered mode, heavier elements should appear brighter in the image. However, all backscattered images presented in this work have been inverted so that the darker spots correspond to the heavier elements, for the better comparison with the secondary images. The backscattered image of the TiN sample proves that after the annealing, Fe has redistributed forming particles in this case as well.

In Figure 5 the correlation between particle size and CNT external diameter is shown. The iron particle size distributions were taken from secondary SEM images of annealed samples, providing the particle size immediately before the beginning of CNT growth. The diameter distribution of CNTs was analyzed from high-resolution TEM images of samples where CNT growth time was fixed to 5 min for Al_2O_3 and TiN samples. For TiO_2, in which case a higher dispersion in nanotube
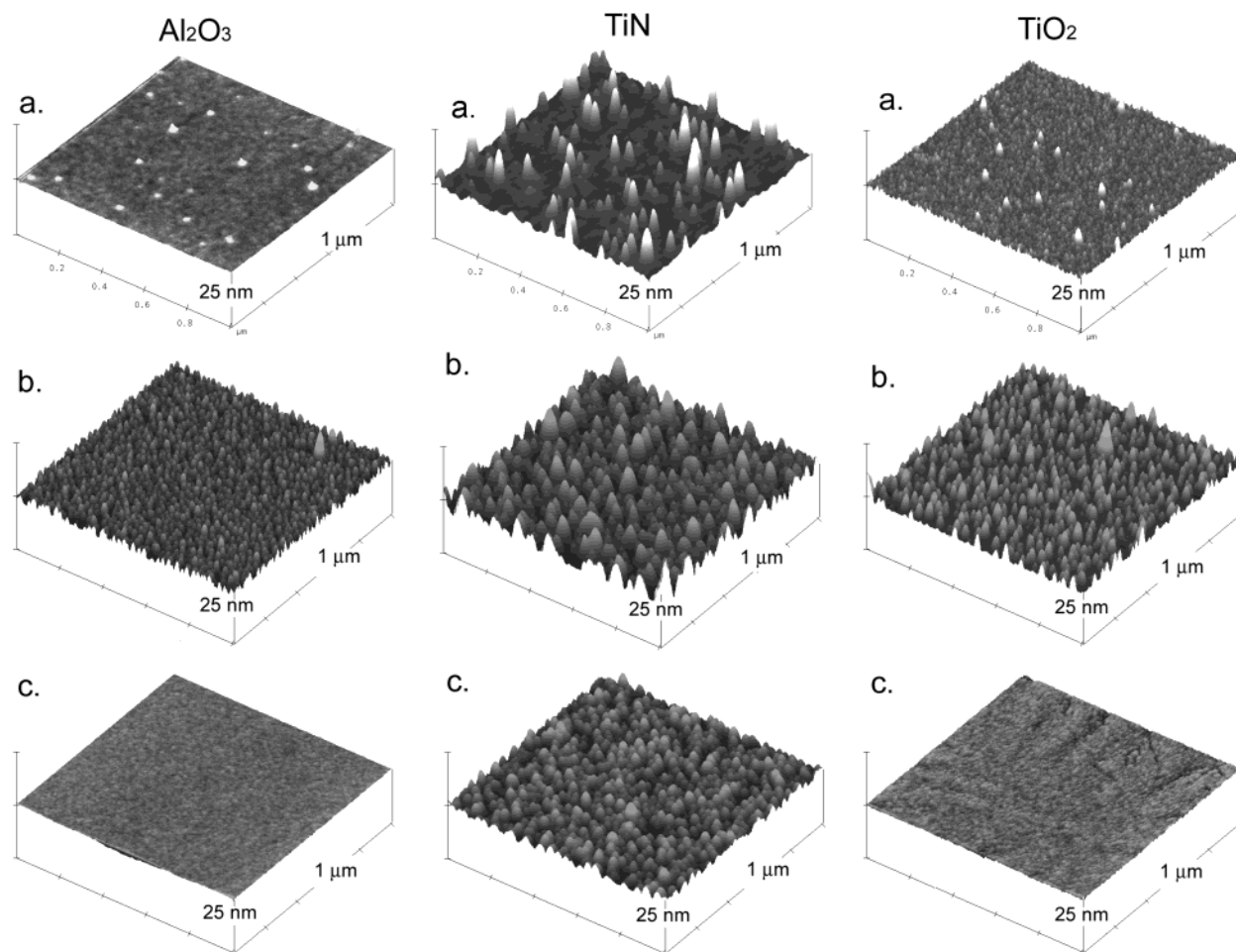
Figure 3. AFM images of Si substrates covered with Al_2O_3, TiN, and TiO_2 buffer layers. (a) Samples after deposition of 1 nm Fe on top. (b) Samples after deposition of 1 nm Fe and annealing to 840 °C during 8 min. (c) Samples annealed without Fe.
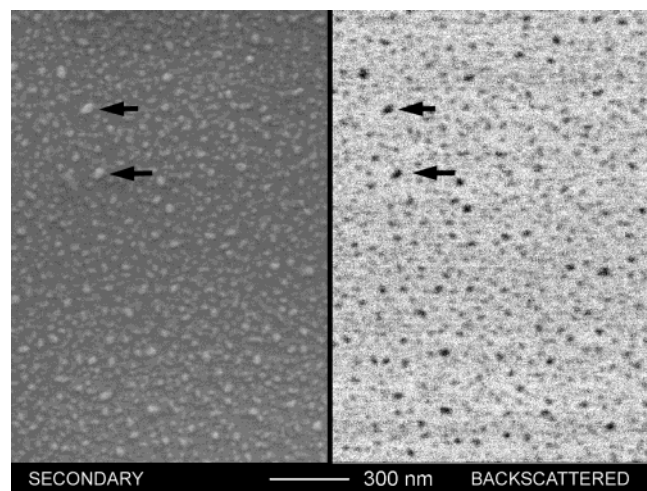

Figure 4. SEM secondary (left) and backscattered (right) images of Si covered with TiN, after deposition of 1 nm Fe and annealing to 840 °C during 8 min. In the backscattered image, the contrast has been inverted so that darker spots correspond to heavier elements, Fe particles in this case.

Figure 5. Comparison of particle and nanotube diameter distributions. The particle diameters have been taken from analysis of SEM secondary images, while CNTs diameters were obtained from TEM images. In all cases, Gaussian curves were used to fit the data. The numbers in the graph indicate the mean values of the Gaussian distributions, with the corresponding widths in parentheses.

diameters was observed, two samples with growth times of 8 and 4 min were taken into account. Both particle and nanotube data were fitted with Gaussian functions, whose mean values and respective widths can be seen in the figure. In the Al_2O_3 and TiN cases, there is a good correlation between the diameter distribution width of particles and CNTs, which points to a one-to-one relationship between the initial catalytic particles formed
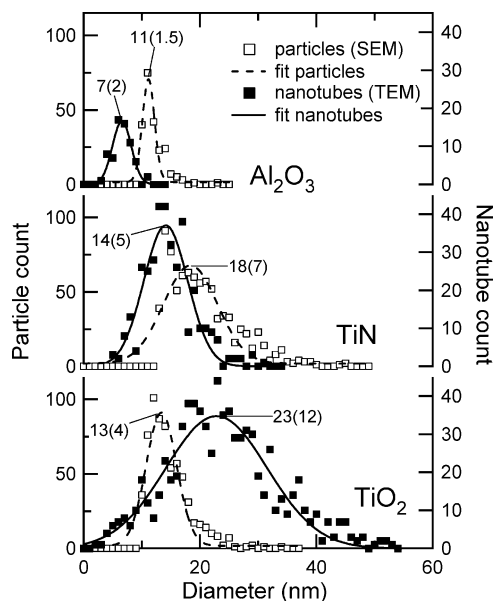
in the annealing step and the nanotubes. However, mean values of nanotube diameters are consistently smaller than the particles.
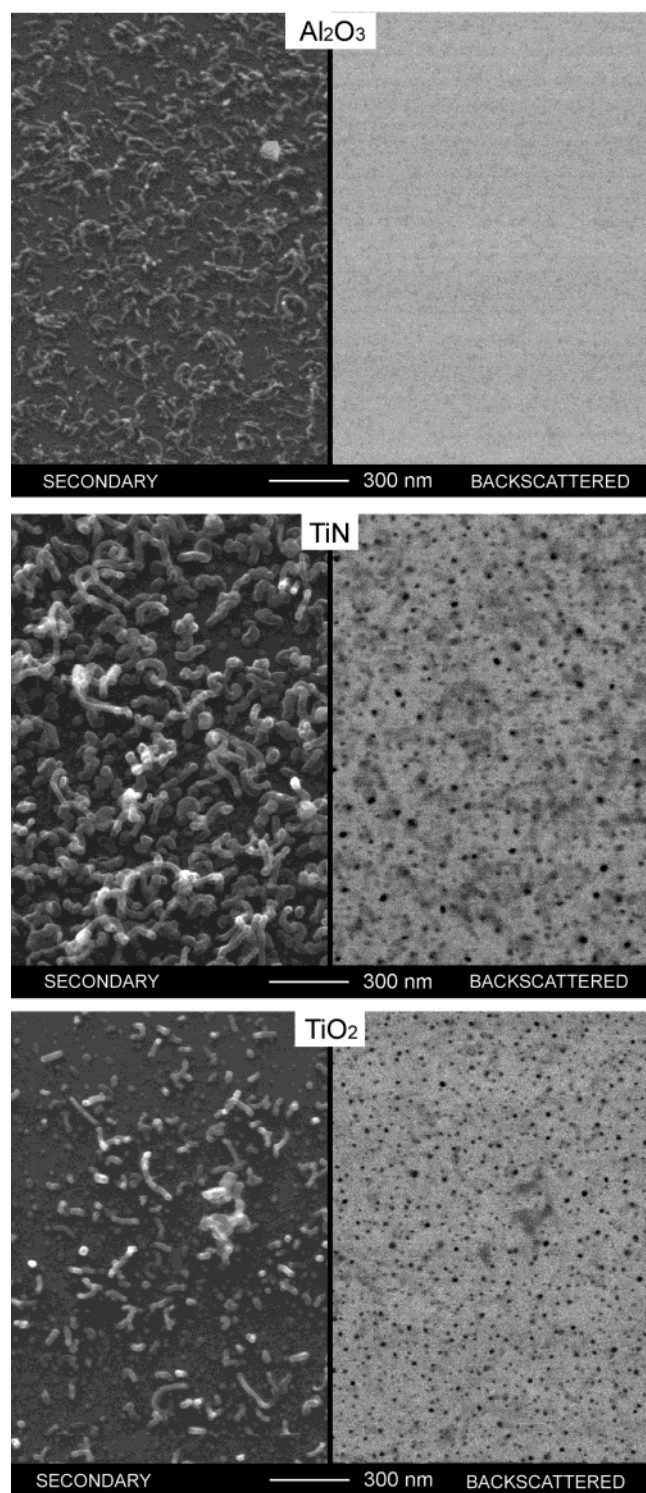
Figure 6. SEM secondary (left) and backscattered (right) images of CNTs grown during 5 s onto Si covered with buffer layers of Al_2O_3, TiN and TiO_2. Fe particles are still visible on the TiN and TiO_2 cases in the backscattered images (inverted contrast).

Since particle and nanotube diameters have been estimated from images taken with different techniques involving different resolution, probably the difference observed does not correspond to a real difference in size. It is feasible that the particle diameters have been systematically overestimated from the SEM images, which were taken practically at the resolution limit of the instrument. In the case of TiO_2 layers, even without taking the possibility of a systematic error in consideration, the CNTs diameter distribution is clearly broader than the original particle
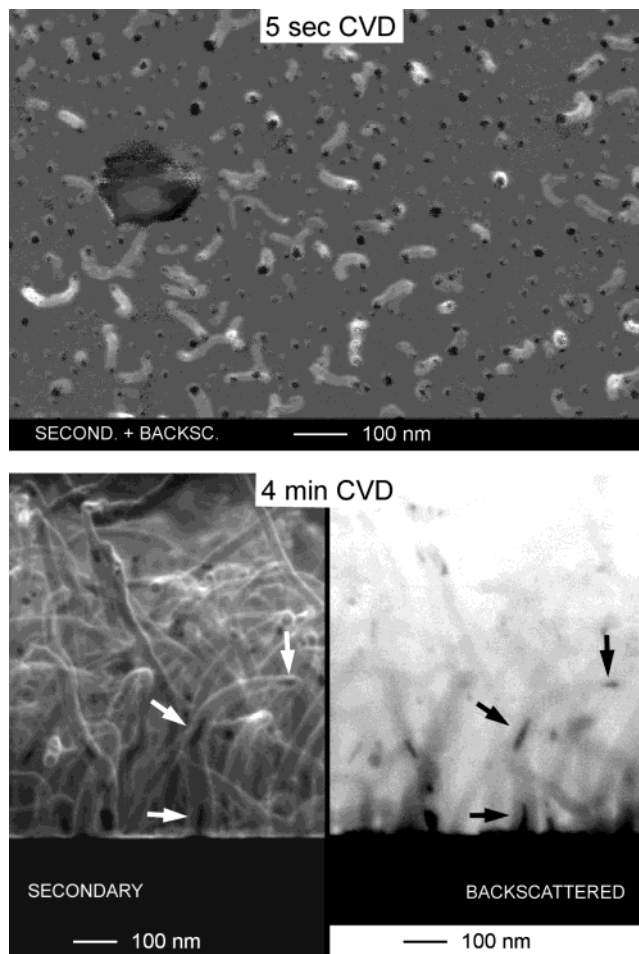

Figure 7. Top*:* Exact superposition of secondary and backscattered (inverted) SEM top view images, corresponding to CNTs grown during 5 s onto Si covered with TiO_2. Bottom*:* Secondary and backscattered (inverted) SEM side view images of CNTs grown during 4 min onto the same kind of substrate, showing the redistribution of the original Fe particles along the hollow core of the nanotubes.

distribution. Taken together with the fact that nanotube growth rate is slower onto these layers (see following section), this could be an indication of particle evolution also during the CVD, and not only during the annealing step.

3.2.2. Early Stage of the CVD Process. In Figure 6 we can see the early stages of CNT growth onto the different layers. These samples have been exposed to C_2H_2 for only 5 s, and they correspond to the samples whose XPS spectra were shown in Figure 2. SEM imaging in the backscattered mode was performed (right-hand side of the images), to find out about Fe particle distribution after CVD. While in the Al_2O_3 case the resolution of the instrument in the backscattered mode was insufficient to establish clearly the presence of particles, in the TiN and TiO_2 case Fe particles (seen as darker spots in the inverted image) can still be clearly distinguished. Additionally, differences in CNT growth rate are already visible.

In the case of the TiO_2, low CNT density allowed an exact superposition of secondary and backscattered images (see Figure 7, top). In this case, it was possible to see a clear one-to-one relationship between Fe particles and nanotubes. Furthermore, it is interesting to note the existence of still isolated Fe particles not involved in CNT growth. These "nonactive" particles could be free to further move on the surface and coalesce to form bigger particles before becoming active for nanotube growth, which would explain the broader CNT diameter distribution observed when TiO_2 layers are used.

TABLE 1: Summary of CNT Characteristics Depending on Fe Chemical State and Buffer Layer Used[a]

buffer layer		Al_2O_3	TiN	TiO_2
Fe chemical state	during annealing	Fe_2O_3	FeO + Fe	
	after CVD	FeO	Fe	
growth rate (μm/min)		5	2	0.2
mean particle diameter (nm)		11	18	13
mean nanotube diameter (nm)		7	14	23
number of walls		1−4	More than 20	
comments		poor wall graphitization	good wall graphitization	
		straight tubes	bent tubes, with inner bamboo-like structures	
		almost no particle inclusions	many particle inclusions	

[a] The information related to growth rate and general comments on the CNTs was taken from samples with growth times of 5 min, which were reported in our previous work.[14]

In the lower part of Figure 7, a thicker CNT film grown onto TiO_2 is shown. Here it is possible to see how the catalyst has distributed inside the tubes by comparing the secondary and backscattered images of the same sample location. During the first stages of the growth, Fe particles can still be recognized as such (top image). However, Fe moves along the hollow core of the tubes in later stages, and it can be found in any location, from root to tip (lower image). This observation is consistent with high-resolution TEM analysis of the tubes grown onto TiO_2 and TiN substrates, where a substantial amount of metallic inclusions are found in random positions inside the tubes (not shown). On the contrary, practically no particles were found inside nanotubes grown onto Al_2O_3 layers with either SEM or TEM.

4. Discussion

With in situ analysis of our samples, we have shown how, for the same experimental conditions, CNTs with different characteristics grow from Fe deposited onto different buffer layers. The results based on the detailed characterization of these CNTs by SEM, TEM, and micro-Raman spectroscopy have been published in our previous work.[14] To facilitate the following discussion, the representative characteristics of the CNTs grown onto our different buffer layers are resumed in Table 1. Although we are not yet in a position to explain the differences observed in terms of a growth model, which will be addressed in future experiments, we can conclude as follows: CNTs can be grown on all three buffer layers, but with very different growth rate and different characteristics. As we have shown, the catalyst Fe suffers different chemical and morphological changes depending on the buffer layer. We attribute these results to the chemical interaction between the catalyst and the buffer layer during the CNT growth process.

4.1. Catalyst Chemical State. From our experimental data, we can conclude that FeO particles are an efficient catalyst for C_2H_2 decomposition. In particular, comparing the growth rate it becomes clear that FeO is catalytically more efficient than Fe. Since we have observed strong differences in the characteristics of CNTs grown from FeO (onto Al_2O_3) and Fe (onto TiN and TiO_2) particles, it is likely that in the first case the CNTs do not follow a growth mechanism related to the diffusion-based models proposed for metallic catalyst particles. Based in our results, we suggest that the decomposition process of C_2H_2 onto Fe and FeO particles could follow different chemical paths with different intermediate species and thermodynamics involved.[21] Unfortunately, there are still few studies addressing the gas chemistry involved in CNT growth.[22] Detailed experiments have to follow in the future, to understand the process involved in the catalytic decomposition of hydrocarbons on transition metals and their oxides.

We have speculated with another possibility that does not contemplate FeO as an active catalyst. The original FeO particle could undergo a localized partial reduction of the oxide particles by species liberated during acetylene decomposition. During the CVD process, the particles would have a structure consisting of a thin active metallic shell where the growth would take place, and an oxidized particle core that could remain inert, its role only being to pin the whole particle to the substrate. In this case, the differences observed with respect to nanotubes growing from pure metallic particles could be explained by the difference between carbon diffusing through a shell (short diffusion paths could explain the faster growth and lesser number of walls) or through a sphere. However, we have no clear experimental evidence supporting this model. Although in some cases traces of Fe can be inferred from a weak shoulder in the lower BE side of the oxide spectrum (see the feature marked with an arrow in Figure 2, case c) the signal is not conclusive.

4.2. Catalyst Morphology. Our SEM (Figure 6) and AFM (Figure 3) results have shown that the catalyst particles formed on Al_2O_3 buffer layer are the smallest. Our XPS data strongly suggest that the interaction between Fe and the buffer layer affects the particle morphology. Hence, for Al_2O_3 the smallest size is correlated with the strongest interaction. We can explain this conclusion as follows: Due to the oxidation process occurring at the catalyst$-Al_2O_3$ interface, the mobility of Fe atoms is strongly hampered on the surface. The fact that the Fe particles remain oxidized even during the exposure to C_2H_2 indicates that the oxidation process is strong and chemically "binds" the Fe particles to the surface. Additionally, no Fe particles were found in the hollow core of CNTs, which corroborates our conclusion.

In case of TiN and TiO_2, XPS data show no or minor interaction with the catalyst. This result is in agreement with the larger particle size observed, as well as with the substantial amount of Fe inclusions found inside the hollow core of the nanotubes. In general, a rough surface such as the one of the TiN film provides more edge sites that can act as sinks for metal diffusion, thus precluding formation of bigger Fe particles as the CVD advances.[23] Fe particles could have more mobility and therefore aggregate to form bigger particles onto the flat annealed TiO_2 film surface. Although we did not follow the particle size evolution once the CVD started, a higher surface mobility of Fe would explain the broader CNT diameter distribution systematically observed in the TiO_2 case.

Our SEM results (see Figure 6 and Figure 7) have clearly revealed that a one-to-one correlation exists between a catalyst particle and a CNT. Therefore, with a diffusion-based model in mind, one could think that small particles should be more active because the diffusion path is shorter. However, the SEM images obtained from TiO_2 do not show a correlation between particle size and reactivity. Currently, the reason some Fe

particles are more "active" than others is still unclear. In any case, we can exclude the particle size dependence.

Comparing nanotubes grown onto TiN and TiO$_2$ buffer layers, CNTs grown on the oxide show slower growth rate and a broader nanotube diameter distribution than CNTs grown onto the nitride. Since in both cases the catalyst particles have the same chemical composition and roughly the same diameter, there is no obvious reason the growth has to be different. A thorough analysis of particle morphology, crystalline state, and orientation with respect to the substrate and contact angle might help to clarify the origin of these differences. Differences in contact angle (wettability) of Fe particles would mean different contact areas with the substrate. In a diffusion-based growth model like the one proposed by Kanzow,[2] the contact area of the particle with the substrate provides a cooler region where precipitation of carbon can take place. A reduced contact surface would therefore result in a slower growth rate. Surface roughness is also believed to play an important role.

Recently, Hu et al. [24] have reported that the relative orientation of crystalline metal particles can be influenced by the substrate. It would be therefore interesting to study the crystallinity and relative orientation of the Fe particles onto TiN and TiO$_2$ substrates. If differences are observed, it would prove that specific relative orientations between C$_2$H$_2$ and the planes of crystalline Fe are more favorable for initiating C$_2$H$_2$ decomposition, as proposed by Lee et al.[25] in a first principles study of the decomposition of acetylene onto Fe.

In conclusion, our results emphasize the importance of the interaction between the catalyst and the buffer layer, which controls the chemistry and morphology of the catalyst particles and consequently the growth and CNT characteristics.

5. Summary

We have shown that differences observed in growth rate and characteristics of CNTs grown by CVD can be related to differences in catalyst chemical state. In our experiments, the final chemical composition of the catalyst after annealing and CVD is controlled by the choice of buffer layer between catalyst and Si substrate, as determined by in situ XPS. Three different buffer layers were investigated: Al$_2$O$_3$, TiO$_2$, and TiN. Metallic Fe transforms to Fe$_2$O$_3$ particles after annealing and evolves to FeO during the CVD onto Al$_2$O$_3$ layers. Buffer layers of TiN and TiO$_2$ on the other hand lead to metallic Fe particles during the CVD process, although the catalyst can partially oxidize during the annealing step. The final chemical state of the catalyst determines in turn the growth mode of CNTs. FeO particles promote dense growth of thin nanotubes with a comparatively fast growth rate. These tubes are straight, poorly graphitized, and have few walls and practically no particle inclusions. On the other hand, Fe particles promote growth of multiwalled nanotubes with better wall quality, although in this case the tubes do not grow straight, but show a high number of kinks and internal bamboo-like structure, with a high amount of metallic inclusions. Additionally, the growth rate is slower than

for FeO particles. There are, however, differences in growth rates between TiN and TiO$_2$ buffer layers that cannot be explained simply by differences in chemical state, which could originate on possible differences in particle morphology and crystalline orientation.

References and Notes

(1) Baker, R. T. K. *Carbon* 1989, *27*, 315−323.
(2) Kanzow, H.; Ding, A. *Phys. Rev. B* 1999, *60*, 11180−11186.
(3) Kim, N. S.; Lee, Y. T.; Park, J.; Ryu, H.; Lee, H. J.; Choi, S. Y.; Choo, J. *J. Phys. Chem. B* 2002, *106*, 9286−9290.
(4) Stewart, I.; Tricker, M. J.; Cairns, J. A. *J. Catal.* 1985, *94*, 360−369.
(5) Emmenegger, C.; Bonard, J.-M.; Mauron, P.; Sudan, P.; Lepora, A.; Grobety, B.; Züttel, A.; Schlapbach, L. *Carbon* 2003, *41*, 539−547.
(6) Baker, R. T. K.; Alonzo, J. R.; Dumesic, J. A.; Yates, D. J. C. *J. Catal.* 1982, *77*, 74−84.
(7) Yuan, L.; Saito, K.; Pan, C.; Williams, F. A.; Gordon, A. S. *Chem. Phys. Lett.* 2001, *340*, 237−241.
(8) Li, Y.; Kim, W.; Zhang, Y.; Rolandi, M.; Wang, D.; Dai, H. *J. Phys. Chem. B* 2001, *105*, 11424−11431.
(9) Choi, H. C.; Kim, W.; Wang, D.; Dai, H. *J. Phys. Chem. B* 2002, *106*, 12361−65.
(10) Mauron, P.; Emmenegger, C.; Züttel, A.; Nützenadel, C.; Sudan, P.; Schlapbach, L. *Carbon* 2002, *40*, 1339−1344.
(11) Homma, Y.; Yamashita, T.; Finnie, P.; Tomita, M.; Ogino T. *Jpn. J. Appl. Phys. Part 2* 2002, *41*, L89.
(12) de los Arcos, T.; Vonau, F.; Garnier, M. G.; Thommen, V.; Oelhafen, P.; Düggelin, M.; Mathis, D.; Guggenheim, R. *Appl. Phys. Lett.* 2002, *80*, 2383.
(13) Homma, Y.; Kobayashi, Y.; Ogino, T.; Takagi, D.; Ito, R.; Jung, Y. J.; Ajayan, P. M. *J. Phys. Chem. B* 2003, *107*, 12161−12164.
(14) de los Arcos, T.; Garnier, M. G.; Oelhafen, P.; Mathys, D.; Seo, J. W.; Domingo, C.; García-Ramos, J. V.; Sánchez-Cortés, S. *Carbon* 2004, *42*, 187−190.
(15) Delzeit, L.; Chen, B.; Cassell, A.; Stevens, R.; Nguyen, C.; Meyyappan, M. *Chem. Phys. Lett.* 2001, *348*, 368−374.
(16) Delzeit, L.; McAninch, I.; Cruden, B. A.; Hash, D.; Chen, B.; Han, J.; Meyyappan, M. *J. Appl. Phys.* 2002, *91*, 6027−6033.
(17) Lee, K. M.; Han, H. J.; Choi, S.; Park, K. H.; Oh, S.; Lee, S.; Koh, K. H. *J. Vac. Sci. Technol. B* 2003, *21*, 623−626.
(18) Mills, P.; Sulliva, J. L. *J. Phys. D: Appl. Phys.* 1983, *16*, 723−732.
(19) Lin, T. C.; Seshadri, G.; Kelber, J. A. *Appl. Surf. Sci.* 1997, *119*, 83−92.
(20) Geng, J.; Schüler, A.; Oelhafen, P.; Gantenbein, P.; Düggelin, M.; Mathys, D.; Guggenheim, R. *J. Appl. Phys.* 1999, *86 (6)*, 3460−3462.
(21) Bell, A. T.; Shustorovich, E. *Surf. Sci.* 1990, *235*, 343−350.
(22) Franklin, N. R.; Dai, H. *Adv. Mater.* 2000, *12(12)*, 890−894.
(23) Ward, J. W.; Wei, B. Q.; Ajayan, P. M. *Chem. Phys. Lett.* 2003, *376*, 717−725.
(24) Hu, M.; Noda, S.; Okubo, T.; Yamaguchi, Y.; Komiyama, H. *J. Appl. Phys.* 2003, *94(5)*, 3492−3497.
(25) Lee, G.-D.; Han, S.; Yu, J.; Ihm, J. *Phys. Rev. B* 2002, *66*, 081403-(R).